Engineering with Computers (2020) 36:915–929
https://doi.org/10.1007/s00366-019-00740-1

ORIGINAL ARTICLE

Numerical study on mechanical and hydraulic behaviour of blast-induced fractured rock

Saba Gharehdash[1] · Luming Shen[1] · Yixiang Gan[1]

Received: 24 September 2018 / Accepted: 18 March 2019 / Published online: 27 March 2019

Abstract
In this research paper, smoothed particle hydrodynamics (SPH) with Johnson Holmquist damage model is adopted for modelling of the blast-induced fractures in Barre granite rock. The permeability of the blast-induced rock is then obtained using the implemented finite volume method code in OpenFOAM. It is found that the calculated permeability depends on the direction of fluid flow and with higher value in radial direction than the axial one. This is mainly due to the higher and larger connected pore network in the radial direction. This research work shows that the adopted SPH method along with finite volume method code can be effectively combined to qualitatively and quantitatively predict the fractured network, to analyse geometry of the fractured network, and to calculate the permeability of blast-induced rock.

Keywords Permeability · Blast · Smoothed particle hydrodynamics · Fractured network · Rock · OpenFOAM

1 Introduction

There is growing interest in predicting the permeability enhancement originated from the blasting in low-permeability geological structures. These predictions would be helpful for applications in reservoir engineering, such as hydrogeology [1] and explosive stimulation of tight gas reservoirs [2], shale gas extraction [3], oil shale [4], geothermal reservoirs [5], and coal gasification [6]. It is well known that energy released during blasting causes damage in the surrounding rocks in the form of micro- to macro-cracks, which increases the permeability of rocks. It is, therefore, of prime importance in reservoir engineering to quantitatively assess the blast-induced fractures as well as the resulting permeability changes in rocks. However, challenges remain in developing experimentally validated computational methods to accurately predict the fracture pattern and estimate hydraulic behaviour associated with blast stimulation.

Experimental studies to elucidate the blast-induced fracture patterns in rocks have been carried out, considering the effects of confining pressure, explosive loading density, explosive type and borehole configurations [7, 8]. Compared to X-ray micro-tomography [9], the visual inspection methods used in these studies can overcome the specimen size limitations while maintaining necessary resolutions for crack networks. The main drawbacks of these methods are that the rock specimen at a certain depth must be cut to obtain the cracking information, and it is difficult to distinguish the differences between pre-existing and blast-induced fractures.

On the other hand, to model blast-induced fractures, various computational methods have been developed and applied, including mesh-based (e.g., finite-element method, FEM [10], extended finite-element method, XFEM [11] and discrete element method, DEM [12]), mesh-free (e.g., smooth particle hydrodynamics, SPH [13]) and coupling methods (e.g., FEM–DEM [14, 15] and DEM–SPH [16]). Since FEM is a mesh-based technique, dealing with the large deformation and post-failure is typically a difficult task, due to mesh distortion issues. Though DEM simulations do not suffer from mesh distortions, the determination and calibration of model parameters such as normal and shear strengths of contact bonds between elements can be somewhat uncertain [17]. The coupling methods can be applied to treat the problem of blast-induced fractures. However, factors such as contact algorithm and mesh ratios between different parts may also affect the solutions. Additionally, mesh-based and coupling methods show certain limitations in validating quantitatively the crack density against controlled experiments [8, 15, 16].

✉ Luming Shen
luming.shen@sydney.edu.au

[1] School of Civil Engineering, The University of Sydney, Sydney, NSW 2006, Australia

Demands for more effective numerical methods are crucial for a reliable quantitative evaluation of the blast-induced fractures in rocks. The mesh-free methods such as SPH [13], element-free Galerkin (EFG) [18], and reproducing kernel particle method (RKPM) [19] can treat large deformation problems involved in impact and blasting of geomaterials. In particular, the SPH has recently become promising for simulating rock fracture and fragmentation under blast load [13]. Under large deformations, SPH simulations reproduce natural damage and fracture patterns by degrading connections between neighbouring particles. Therefore, simulations of fractures in arbitrary and complex paths under the blasting load can be properly performed without additional processes, suggesting that SPH could be a suitable tool for studying blast-induced fractures in rocks both qualitatively and quantitatively [20].

On the other hand, the hydraulic behaviour of fractured rocks has been studied experimentally using the triaxial cell to determine the permeability of rocks with induced fractures [21, 22]. Although these laboratory flow experiments can provide information on the permeability of rocks, technical constrains lead to only small-scale specimens. Moreover, there is limited experimental investigation on the hydraulic behaviour of rocks with blast-induced fractures.

To calculate the permeability of fractured rocks, computer-assisted techniques have been utilised to develop reliable fluid flow simulations, such as finite-element [23], lattice Boltzmann [24], pore network models [25], and computational fluid dynamics (CFD) [26]. However, all of these methods require certain 3D complex fracture networks as inputs [27]. Under the framework of the open-source simulation code OpenFOAM [28], the pore and throat geometry can be reconstructed from the simulated fractured network, to handle the complex three-dimensional grids and model the fluid flow in porous media [29]. OpenFOAM code has been widely used for CFD applications, from hypersonic [30] to compressible Navier–Stokes [31]. Traditionally, the computational modelling is often limited to simulate fluid flow inside the reconstructed pore space from the high-resolution images of rocks [32]. However, the extraction of pore networks from a three-dimensional image involves ambiguities [32]. It is not easy to capture all of the information related to the pore space geometries as it is highly dependent on the resolution of images. In the current research, the reconstructed pore space geometry can be obtained from the experimentally validated SPH simulations.

Despite recent work on rock blast fracturing, a complete understanding of the relationship between the applied blasting load, the resulting fractured network and hydraulic conductivity has yet to be achieved. In addition, although many fluid flow simulations have investigated natural rock fractures [33], there are very few studies that have been dedicated to the issue of flow in blast-induced fractures in rock. In the present work, a 3D numerical simulation using SPH has been performed to simulate the fracture patterns in rock under different blast conditions. The pore network geometry and permeability of the fractured rock are then analysed using OpenFOAM as the main flow solver. The present work represents, to our knowledge, the first attempt to report a complete computational procedure that can predict both the fractured network and permeability of the rock resulted from blast.

2 Methodology

2.1 Simulation of rock under blast

2.1.1 Smoothed particle hydrodynamics formulation

Smoothed particle hydrodynamics (SPH) is a Lagrangian-based numerical method used for simulating problems in fluid and solid mechanics. SPH was first developed to simulate non-axisymmetric phenomena in astrophysical dynamics [20] and has since been employed within numerous branches of computational physics [34].

The SPH method is considered as an interpolation method using the sifting property of the Dirac-delta function. Consider a function f and a kernel W which has a width (support domain) determined by the parameter h. We define the kernel estimate as

$$\langle f(\boldsymbol{x})\rangle = \int_{\Omega}^{p} f(\boldsymbol{x}_j) W(\boldsymbol{x}-\boldsymbol{x}_j,\ h)\mathrm{d}\boldsymbol{x}_j, \tag{1}$$

where $\boldsymbol{x}_j$ is the position vector of the particle j and h is the smoothing length. If we convert the above integral to a sum, then the discrete kernel estimate becomes the summation over neighbouring particles and the particle i itself as

$$\langle f(\boldsymbol{x})\rangle \cong \sum_{j=1}^{n} \frac{m_j}{\rho_j} f(\boldsymbol{x}_j) W(\boldsymbol{x}-\boldsymbol{x}_j,\ h), \tag{2}$$

where m_j is the mass of particle j, ρ_j is the density of particle j, and n is the number of particles within the support domain of the kernel function. Particle equation for the gradient can be obtained as

$$\langle \nabla f(\boldsymbol{x})\rangle \cong -\sum_{j=1}^{n} \frac{m_j}{\rho_j} f(\boldsymbol{x}_j) \nabla W(\boldsymbol{x}-\boldsymbol{x}_j,\ h). \tag{3}$$

Equations (2) and (3) and their derivatives provide an approximation to the continuum equations and form the basis of SPH. The transformation of the conservation

equations of continuum mechanics into particle equations yields the following discretised SPH equations:

$$\frac{\mathrm{d}\rho_i}{\mathrm{d}t} = \rho_i \sum_j \frac{m_j}{\rho_j}(\boldsymbol{u}_j - \boldsymbol{u}_i)\cdot\nabla_i W_{ij}, \tag{4}$$

$$\frac{\mathrm{d}\boldsymbol{u}_i}{\mathrm{d}t} = \sum_j m_j\left(\frac{\boldsymbol{\sigma}_i}{\rho_i^2} + \frac{\boldsymbol{\sigma}_j}{\rho_j^2}\right)\cdot\nabla_i W_{ij}, \tag{5}$$

$$\frac{\mathrm{d}e_i}{\mathrm{d}t} = \frac{1}{2}\sum_j m_j(\boldsymbol{u}_j - \boldsymbol{u}_i)\cdot\left(\frac{\boldsymbol{\sigma}_i}{\rho_i^2} + \frac{\boldsymbol{\sigma}_j}{\rho_j^2}\right)\cdot\nabla_i W_{ij}, \tag{6}$$

where the dependent variables are the scalar density ρ and specific internal energy e, the velocity vector $\boldsymbol{u}$, and the stress tensor $\boldsymbol{\sigma}$. Independent variables are the spatial position $\boldsymbol{x}$ and the time t. The $(\mathrm{d}/\mathrm{d}t)$ is the material derivative. Density, velocity and internal energy change of particle i are obtained by Eqs. (4)–(6), respectively. In this paper, we use the cubic spline function, developed by Monaghan [35], which is given in the following form:

$$W_{ij} = \alpha_\mathrm{d} \times \begin{cases} \frac{2}{3} - q^2 + \frac{1}{2}q^3 & 0 \le q < 1 \\ \frac{1}{6}(2-q)^3 & 1 \le q < 2 \\ 0 & q \ge 2 \end{cases}, \tag{7}$$

where α_d is the dimension-dependent constant related to the smoothing length with $\alpha_\mathrm{d} = \frac{3}{(2\pi h^3)}$ in the three-dimensional space, and q is the normalized distance between particles i and j, and is defined as $q = \frac{r_{ij}}{h} = \frac{|\boldsymbol{x}_i - \boldsymbol{x}_j|}{h}$. For more comprehensive details on SPH method, one can refer to [35].

2.1.2 SPH-related parameters

In the present study, SPH algorithm in the hydrocode LS-DYNA [36] is adopted to model the rock behaviour under blast loading. Dealing with discontinuities in the material due to shock waves and stress wave propagation requires special methods. The discontinuity problem is usually solved by adding extra artificial viscous terms into the momentum (Eq. 5) and energy (Eq. 6) equations as follows:

$$\frac{\mathrm{d}\boldsymbol{u}_i}{\mathrm{d}t} = \sum_j m_j\left(\frac{\boldsymbol{\sigma}_i}{\rho_i^2} + \frac{\boldsymbol{\sigma}_j}{\rho_j^2} - \Pi_{ij}\boldsymbol{I}\right)\cdot\nabla_i W_{ij}, \tag{8}$$

$$\frac{\mathrm{d}e_i}{\mathrm{d}t} = \frac{1}{2}\sum_j m_j(\boldsymbol{u}_j - \boldsymbol{u}_i)\cdot\left(\frac{\boldsymbol{\sigma}_i}{\rho_i^2} + \frac{\boldsymbol{\sigma}_j}{\rho_j^2} - \Pi_{ij}\boldsymbol{I}\right)\cdot\nabla_i W_{ij}, \tag{9}$$

where $\boldsymbol{I}$ is unit matrix, the Π_{ij} term represents the artificial viscosity and the summations are over neighbouring j particles. In this study, we used artificial viscosity Π_{ij} term introduced by Monaghan [35] as follows:

$$\Pi_{ij} = \begin{cases} \frac{-\alpha\bar{c}_{ij}\lambda_{ij} + \beta\lambda_{ij}^2}{\bar{\rho}_{ij}} & \boldsymbol{u}_{ij}\cdot\boldsymbol{x}_{ij} < 0 \\ 0 & \boldsymbol{u}_{ij}\cdot\boldsymbol{x}_{ij} \ge 0 \end{cases}, \tag{10}$$

$$\lambda_{ij} = \frac{h_{ij}\,\boldsymbol{u}_{ij}\cdot\boldsymbol{x}_{ij}}{\left|\boldsymbol{x}_{ij}\right|^2 + 0.01h^2}, \tag{11}$$

where $\bar{c}_{ij} = \frac{1}{2}(c_i + c_j)$, $\bar{\rho}_{ij} = \frac{1}{2}(\rho_i + \rho_j)$, $h_{ij} = \frac{1}{2}(h_i + h_j)$, $\boldsymbol{u}_{ij} = (\boldsymbol{u}_i - \boldsymbol{u}_j)$, and $\boldsymbol{x}_{ij} = (\boldsymbol{x}_i - \boldsymbol{x}_j)$. The parameters α and β are constants, c represents the speed of sound of the material. The quadratic viscosity term is only dominant in high-gradient regions such as shock front, while the linear viscosity term dominates in low-gradients regions [35]. In our experience, taking $\alpha = 1$ and $\beta = 10$ for blast loading is found to be effective in smoothly spreading out shocks into rock particles.

In this study, the Gray et al. approach [37] is adopted to prevent clumping of the neighbour particles to each other, also known as tensile instability. The basic concept is to establish an artificial repulsive force in the neighbourhood of SPH particles in tension. The repulsive force is introduced into the momentum equation in the form of an artificial stress term. The modified momentum equation takes the following form:

$$\frac{\mathrm{d}\boldsymbol{u}_i}{\mathrm{d}t} = \sum_j m_j\left(\frac{\boldsymbol{\sigma}_i}{\rho_i^2} + \frac{\boldsymbol{\sigma}_j}{\rho_j^2} - \Pi_{ij}\boldsymbol{I} + (\boldsymbol{R}_{\varepsilon i} + \boldsymbol{R}_{\varepsilon j})f_{ij}^b\right)\cdot\nabla_i W_{ij}, \tag{12}$$

where $\boldsymbol{R}_{\varepsilon i}$ and $\boldsymbol{R}_{\varepsilon j}$ are artificial stress terms of particles i and j, respectively, b is an exponent dependent on the smoothing kernel, and f_{ij} is defined as

$$f_{ij} = \frac{W_{ij}}{W(\Delta d,\, h)}, \tag{13}$$

where Δd is initial particle spacing. In this study, h is assumed to be 1.2 Δd for the cubic spline kernel. To eliminate the tensile instability of the SPH particle in the rock, exponent b is determined to be 4 and after some testing $\varepsilon = 0.5$ is chosen [37].

Moreover, special treatment is needed to avoid interface effects for the simulation of different materials. To solve this problem, a penalty-based node to node contact model is defined on the interfaces of the different SPH parts [38]. In the penalty-based contact model, after identifying the contact and penetration a restoring contact force is applied to resist, and ultimately to eliminate the penetration. For

the penalty-based contact model, the repulsive contact force acts along the centre line of the two contacting particles. In this contact model, the penalty force ($\boldsymbol{f}_i$) is defined as [38]:

$$\boldsymbol{f}_i = K_{\mathrm{p}} \sum_{j=1}^{n} \frac{m_j}{\rho_i \rho_j} W_{ij} \frac{\boldsymbol{x}_{ij}}{r_{ij}^2}, \tag{14}$$

where K_{p} is penalty scale factor and can be calibrated by numerical simulations. The penalty force is applied to interfacial particles that are within the affecting region of each other. After careful numerical testing, suitable values for the penalty scale factors between different interacting parts can be obtained. Table 1 shows the final values of K_{p} used for the three SPH simulations.

Table 1 Penalty scale factors after numerical adjustment for different SPH parts

Penalty scale factor for different SPH parts (K_{p})	Simulations		
	Air coupling with copper	Air coupling without copper	Water coupling with copper
PETN/polyethylene (K_{p1})	0.2	0.2	0.2
Polyethylene/air (K_{p2})	0.6	0.6	–
Polyethylene/water (K_{p2})	–	–	0.2
Air/copper (K_{p3})	0.8	–	–
Water/copper (K_{p3})	–	–	0.5
Air/rock (K_{p3})	–	0.8	–
Copper/rock (K_{p4})	0.3	–	0.3

2.1.3 Simulation setup for the rock blast experiment

In the SPH simulations of the rock blasting experiment reported in Ref. [8], a cylindrical Barre granite containing a line source of explosive located in the centre coupling with different medium is considered. Figure 1 shows the three-dimensional view of the rock specimen with a scaled closeup of the borehole region for air coupling with copper simulation, as an example. The cylindrical rock measures 144 mm in diameter and 150 mm in height. The borehole diameter is 6.45 mm. The line source of explosive contains a core load of PETN explosive (1.65 mm in diameter) surrounded by a thin sheath of polyethylene, with the total diameter of 4.5 mm. The coupling material of water or air is used in the blast simulations. A copper tube with 1.2 mm thickness is inside the borehole of rock specimen. The copper tube can be deformed easily without tearing under the applied blast load, thereby preventing any gas penetration into the resulting cracks of rock. Therefore, it should be noted that only the effect of the stress wave in the generation of the rock fracture is considered and the explosive gas flow does not directly affect the formation of the blast-induced fractures in rock. The bottom, top and side surfaces of the rock cylinder are set as free boundaries. The location of the detonation points is set at the top of the blast hole. Table 2 shows all the combinations of the borehole diameter, explosive and coupling materials used in the simulations.

2.1.4 Material models

In the SPH simulations, Johnson–Holmquist constitutive model (JH2) [39] is used to model Barre granite rock. This

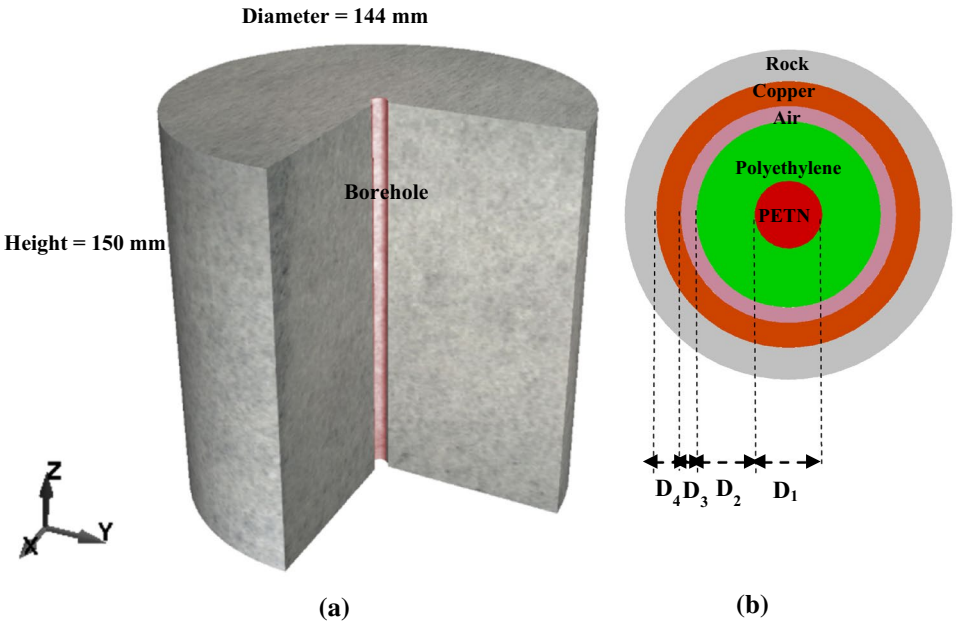

Fig. 1 A cylindrical rock specimen under blast load. **a** 3D view, **b** cross-sectional view of the borehole

Table 2 Different combinations of explosive, coupling material and borehole diameter

Materials inside of borehole		Air coupling with copper (mm)	Water coupling with copper (mm)	Air coupling without copper (mm)
PETN	D_1	1.65	1.65	1.65
Polyethylene	D_2	1.425	1.425	1.425
Air	D_3	0.375	–	0.975
Water		–	0.375	–
Copper	D_4	0.6	0.6	–

damage model takes the pressure and strain rate effects into consideration, and allows the softening of the material after reaching the peak stress. The JH2 model contains the intact and the fractured rock's strengths, a polynomial equation of state, and a damage model that describes the material state from intact to fractured condition. Damage level of the material (D between 0 and 1) can be obtained from this model. A detailed description of the model can be found in Ref. [39].

The material properties of the Barre granite rock for blast simulation are obtained from [8]. Under blast loading, Barre granite rock may experience strain rate up to 1000 s^{-1} or higher [40]. Hence, rate-dependent adjustment on the JH2 model parameters needs to be performed. Using the obtained experiment results by Ranjan from Split Hopkinson Pressure Bar tests [40], strain rate effect is considered to obtain better prediction of Barre granite rock behaviour under the blast loads. The material constants for the JH2 model reported in reference [8] are revised accordingly in the present study to better fit the blast experiment results reported in Ref. [8]. In his work, Dehghan Banadaki calibrated the strength constants A and N using the uniaxial compressive strength of 167 MPa at axial strain rate of 4.63×10^{-5} s^{-1} [8]. In this study, strength constants A and N are modified using the measured uniaxial compressive strength of 357 MPa at axial strain rate of 300 s^{-1} [40], following the same calibration procedure outlined in Ref. [8].

Constant B of the fractured rock is considered to be one-third of constant A, and constant M is assumed to be the same as constant N [8]. However, it should be noted that in the absence of appropriate experimental data for fully fractured Barre granite rock, some of the constants (e.g. D_1 and D_2) are determined by adjusting numerical simulations to match the fracture patterns of experimental observation. Table 3 shows the set of parameters used in our SPH simulations.

Johnson–Cook model [41] is used to describe the copper. This model requires an equation of state (EOS) to be incorporated to represent the behaviour of the copper under different phases. Here, for copper under shock load shock EOS is used [8] as described below:

Table 3 The calibrated values of JH2 model parameters for Barre granite rock

A	N	B	M	D_1	D_2
1.032	0.72	0.344	0.72	0.007	0.9326

$$U_s = S_0 + su_p, \tag{15}$$

where U_s is the shock wave velocity, S_0 is the bulk sound speed of the material, u_p is the particle velocity and s is a material constant. Material Type 9 of LS-DYNA (*MAT_NULL) [36] is used for air, water and polyethylene. As for the air, a polynomial EOS is employed, with the pressure P being expressed as

$$P = C_0 + C_1\gamma + C_2\gamma^2 + C_3\gamma^3 + (C_4 + C_5\gamma + C_6\gamma^2)E, \tag{16}$$

where E is the specific internal energy per volume. The compression of the material is defined by the parameter $\gamma = \frac{\rho}{\rho_0} - 1$, where ρ and ρ_0 are the current and initial densities of the material, respectively. As a matter of fact, the air is often modelled as an ideal gas by setting $C_0 = C_1 = C_2 = C_3 = C_6 = 0$ and $C_4 = C_5 = 0.401$. Air mass density ρ_0 and initial internal energy E_0 are set to be 1.255 kg/m^3 and 0.25 J/cm^3, respectively [8]. For the water and polyethylene (sheath of the detonating cord) in the immediate vicinity of the explosive charge, shock EOS is used. The values of S_0 and s for copper, water and polyethylene are found in reference [8].

The explosive PETN is modelled using explosive burn constitutive model (*MAT_HIGH_EXPLOSIVE_BURN) [36]. For the detonation-produced explosive gas, the standard Jones–Wilkins–Lee (JWL) equation of state is employed, which corresponds to a detonation velocity of 6690 m/s and a Chapman–Jouget (C–J) pressure of 16 GPa [8]. The pressure of the explosive gas can be calculated as

$$P = A_1\left(1 - \frac{\omega\eta}{R_1}\right)e^{-\frac{R_1}{\eta}} + B_1\left(1 - \frac{\omega\eta}{R_2}\right)e^{-\frac{R_2}{\eta}} + \omega\eta\rho_0 E, \tag{17}$$

where η is the ratio of the density of detonation products to the initial density of the original explosive, E is the specific internal energy per unit volume, and A_1, B_1, R_1, R_2 and ω are fitting coefficients. The values of these coefficients can be also found in reference [8].

2.2 Permeability calculation

The permeability is one of the most important properties of fractured porous media. Permeability of the Barre granite cylinder with cracks induced by blast loading is evaluated based on the fracture network obtained using the SPH

simulation. The pore-scale flows are then simulated using the finite volume method implemented in the open-source code OpenFOAM [28].

2.2.1 Geometry and connectivity evaluation of fractured rock

The three-dimensional geometry and connectivity of the pore space controls the hydraulic transport behaviour of rocks. The geometry of the fracture network can be characterised by the throat cross-sectional area size and pore network distribution probability. In this study, we use the pore network algorithm developed by Dong and Blunt [32] to extract the geometry of the pores and throats network as well as their interconnectivity from the blasted specimens. This algorithm presents a versatile, rigorous, and efficient methodology for extracting various geometric and topological parameters of 3D discrete porous media. The algorithm method easily and unambiguously identifies pores and throats and has been validated for different applications such as regular cubic pore networks and irregularly shaped 2D and 3D pore networks generated by stochastic simulation. The algorithm designed to take a three-dimensional digitized space as input [28].

2.2.2 Mathematical model for flow in fractured media

To estimate the permeability, it is crucial to compute the velocity field within the void space of the fractured medium. The velocity profile of the fluid flowing through the fractured medium can be obtained by solving the basic equations of fluid mechanics, namely the Navier–Stokes equations as given below:

$$\nabla \cdot \boldsymbol{u} = 0, \tag{18}$$

$$\rho\left(\frac{\partial \boldsymbol{u}}{\partial t} + \nabla \cdot (\boldsymbol{u} \otimes \boldsymbol{u})\right) = -\nabla p + \mu \nabla^2 \boldsymbol{u}, \tag{19}$$

where $\boldsymbol{u}$ is the velocity vector, and the term ∇p refers to the pressure gradient, μ is the dynamic viscosity coefficient, and the term $\nabla^2 \boldsymbol{u}$ is the vector Laplacian. We are interested in the steady-state solution of Eq. (19), i.e., $\frac{\partial \boldsymbol{u}}{\partial t} = 0$. To predict the permeability of the fractured media, the estimated flow rate and applied pressure gradient from the CFD model is used in the following Darcy's law:

$$\boldsymbol{u} = -\frac{\mathbf{K}}{\mu} \cdot \nabla p. \tag{20}$$

In anisotropic systems, the permeability $\mathbf{K}$ in the form of a tensor is usually adopted to describe the directional flow variation in the fractured media. Boisvert et al. [42] showed that anisotropic permeability is an important issue in reservoir engineering and oil recovery applications. In many rocks, the permeability depends on the direction [21]. Since our rock specimen is cylindrical, we consider the permeability in the axial (Z) and radial (R) directions.

2.2.3 Permeability evaluation of fractured rocks

The proposed OpenFOAM-based method [28] can be applied on three dimensions with the large and complex geometry data obtained from the SPH simulations. In this process, the geometry of the fractured rock specimen is divided into large numbers of discretization elements and those that contain damaged particles are referred as void, and those that contain undamaged particles are referred as solid. The segmentation of the 3D numerical simulation into solid phase and void phase allows us to study the hydraulic properties of the connected fracture network [28]. Using the Simple-Foam algorithm solver in OpenFOAM [28], we are able to examine the key features of the flow fields within the blasted specimen.

Permeability property is usually determined by measuring the pressure drop associated with the flow of a viscous fluid through the medium. To regulate a flow regime, a constant pressure drop is imposed between the inlet and outlet boundaries of the model and the flow rate will be low enough to make sure that the inertia effect is negligible.

In the simulations, two different numerical configurations are used to determine the specimen permeability, i.e. radial flow and axial flow. These configurations mainly differ in the boundary conditions used for the evaluation of the flow at the pore scale. In both configurations, a no-slip (zero normal and tangential velocity) boundary condition is imposed at the solid surface. It should be noted that the borehole in the axial flow simulation is considered as solid phase since the borehole is not induced by blast loading and cannot be considered as a part of blast-induced fractures.

The fluid is considered incompressible and inviscid, and the flow is isothermal. In this study, water is set as the working fluid with viscosity $\mu = 8.90 \times 10^{-4}$ 10^{-4} Pa s and density ρ =1000 kg/m^3. The flows are driven by a pressure difference of 6 kPa in the axial direction applied between the top (inlet) and the bottom (outlet) of the specimen, and 3 kPa in the radial direction applied between the borehole (inlet) and side surface (outlet) of the specimen. Pressure gradient along the length and radius of cylinder is 0.04 MPa/m.

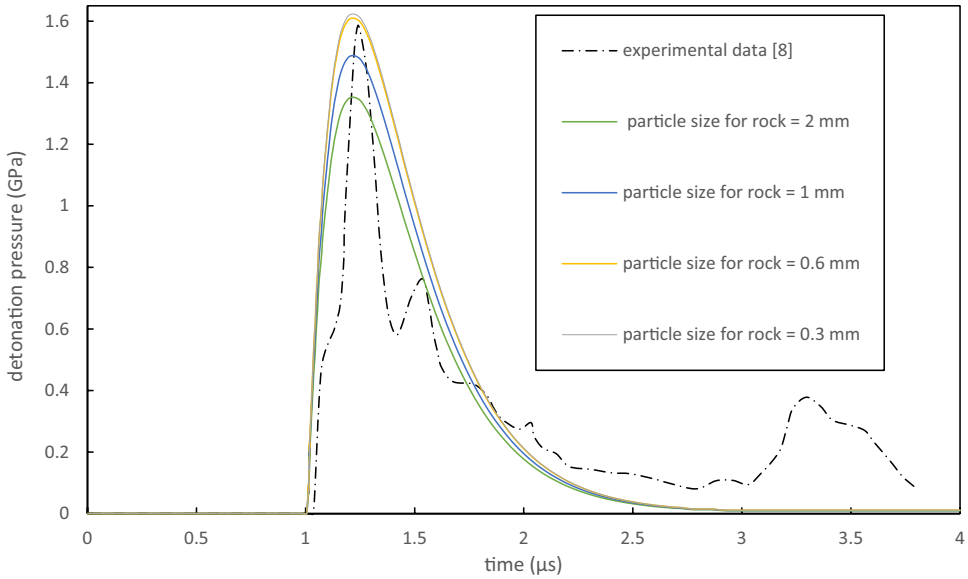

Fig. 2 Detonation pressure time history calculated with different particle size for rock and particle size of 0.15 mm for other materials

3 Validation and demonstration of SPH simulations

3.1 Particle size convergence study

A particle size convergence study is conducted first. To investigate the effect of the particle size on the results, we have increased the number of particles by refining the particle size from 1 to 0.1 mm for copper, air, water, polyethylene and PETN (material inside the borehole) and 4–0.3 mm for the rock cylindrical model as illustrated in Fig. 1. In Fig. 2 we have plotted the simulated detonation pressure history at the middle cross section with different particle sizes. The position of measurement point is located at 80 mm from the top surface of the specimen and has a distance of 11 mm from the borehole wall. It can be noticed from Fig. 2 that the detonation pressure history is very similar for rock particles with sizes of 1, 0.6 and 0.3 mm for blast simulations. The smaller the size of SPH particle the better the simulation converges to the experimental data. After considering the balance between accuracy and efficiency, the particle size 0.6 mm for rock and 0.15 mm for copper, air, polyethylene and PETN are used in all the simulations below, resulting in a total of 8,213,732 particles in the simulation domain.

3.2 Simulation results of blast testing

Simulations of three different scenarios for rock under blast loading, as described in Table 2, are performed. In this section, we first use the detonation pressure profile results for the air-coupling with copper case to validate the proposed SPH simulation. We then analyse the simulated blast-induced crack patterns for all the three cases, which will be later used for the permeability calculations in Sect. 4.

As shown in Fig. 3, the peak detonation pressures as a function of distance from the borehole obtained from experiments and arbitrary Lagrangian Eulerian (ALE) method simulation [8] are compared with the results from our SPH simulation. As can be seen from the figure, the detonation pressure distribution simulated using the proposed SPH model matches the experimental data quite well. To further validate our SPH simulations with the experimental data, damage distribution around the borehole is examined qualitatively.

Figure 4 shows the comparison of the corresponding fracture patterns obtained from the experiment and the proposed SPH simulations. It can be seen from the figure that the explosion induced intensive stress wave travels into the rock specimen and causes different types of failure, and the fracture patterns simulated by the SPH qualitatively match the experimental observations.

To quantify the variations of crack patterns in their experimental tests [8], crack density, defined as the length of cracks per unit area, was calculated at different depths and radial distances from the specimen borehole. In their experiment [8], the fractured rock stimulated using air-coupling with copper was cut at the distance 25 mm, 75 mm and 125 mm from the bottom surface of the rock specimen and the fracture pattern in each section was scanned using the epoxy dye impregnation and digital photography. Each image was then calibrated spatially and divided into three equal-width zones from the centre to the edge with zone 1 located at the centre and zone 3 at the edge. Crack densities were then calculated by dividing the total length of all the cracks in each zone by the zone area.

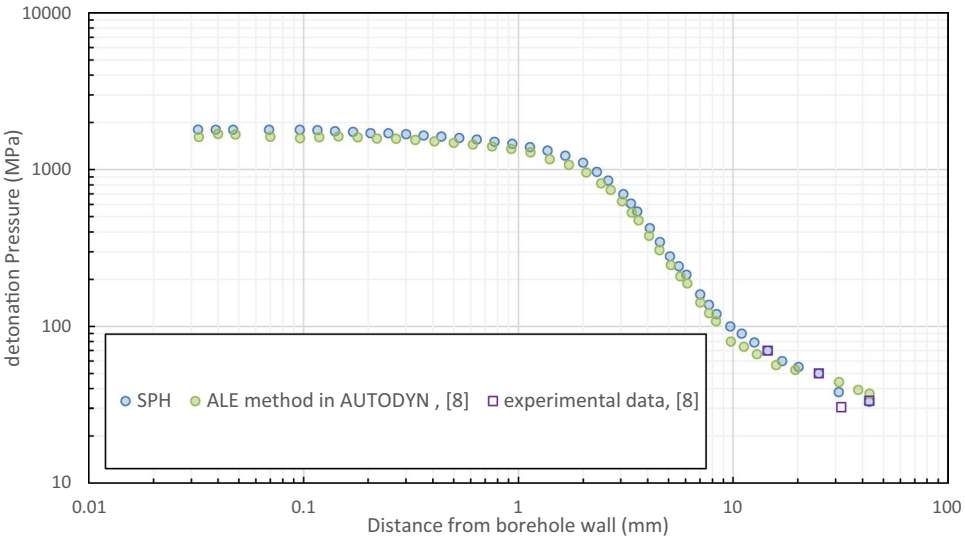

Fig. 3 Comparison of peak detonation pressures at different distances from the borehole wall obtained from the experimental and numerical works at the depth of 80 mm from the top surface of specimen

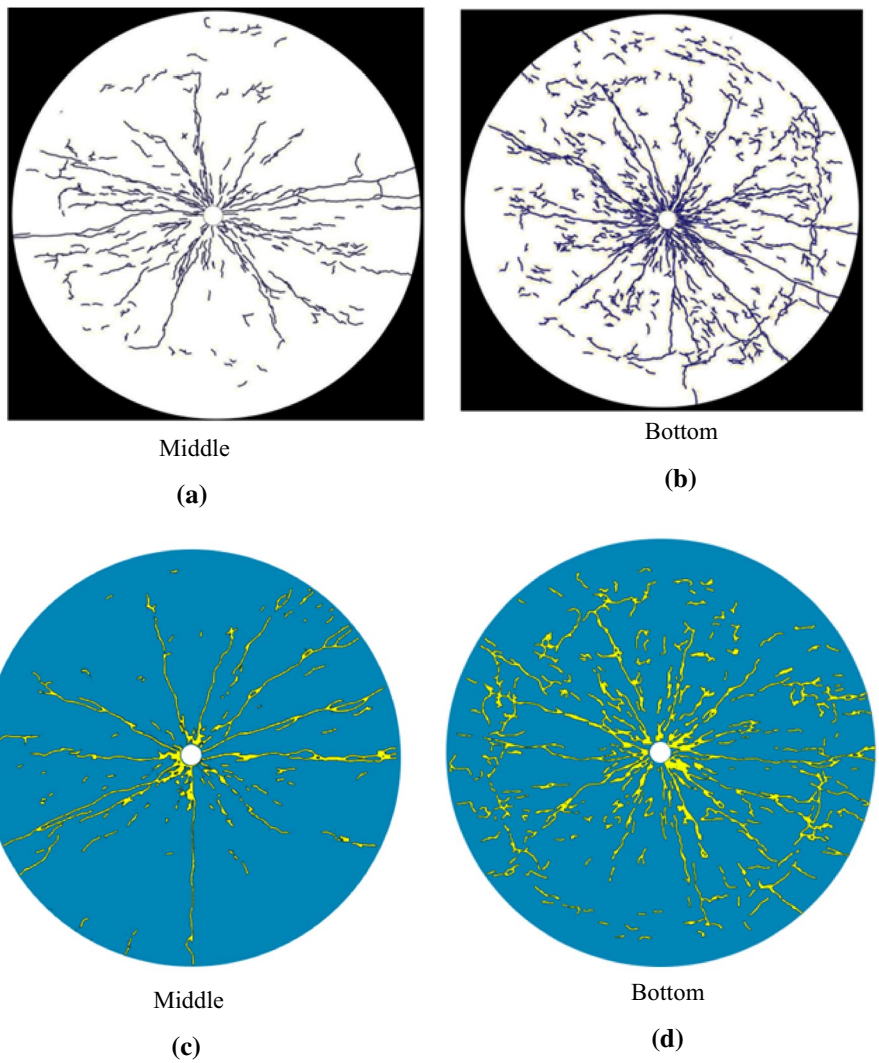

Fig. 4 Comparison of damage created around the borehole at the middle and bottom sections obtained from, **a, b** the experiment [8] and **c, d** the SPH simulation

In calculating the crack density in the proposed SPH simulations, each SPH particle is considered to occupy the space of a cube with edge length of 0.6 mm. To compare SPH simulations for air coupling with copper case, each cross section is divided into the three ring sections from the edge of borehole to the edge of rock specimen as performed in the experimental work. For the air coupling without copper and water coupling with copper cases, each cross section is divided into 19 ring sections to obtain the smooth trend of crack density changes along the radial direction. The following equation is used to calculate the crack density in the simulated specimen:

$$\Gamma = \frac{L \times \sum_i^{n_j} D_i}{A_j}, \tag{21}$$

where Γ, D_i, L, n_j and A_j are crack density, the damage level of particle i, the length of particle i, the number of damaged particles in section j and the area of section j, ($j = 1, \ldots, 19$) respectively. Crack densities were measured in terms of mm/mm^2. In this work, any particle with damage level $D > 0.8$ is considered as crack. The three cross-sectional surfaces at the distance 25 mm (bottom), 75 mm (middle) and 125 mm (top) from the bottom are considered for crack density analysis.

Figure 5 shows the distribution of the measured crack density for the air coupling with copper case in the top, middle and bottom surfaces of the rock specimen, respectively. Investigation of the crack patterns on cross sections of the rock (see Fig. 5) reveals that by moving from the top to the bottom of the specimen, the crack density increases. This is mainly resulted from the higher P-wave velocities in distances far from the detonation point due to the wave superposition phenomenon. As investigated by other researchers [15], there is a direct relation between peak P-wave particle velocities and crack density and the higher peak P-wave particle velocity the higher crack density.

Figure 5 compares crack density results between SPH and ALE method [8] simulations and experimental results [8] in the three divided zones. The ALE method simulations [8] were only performed in the middle cross section. As can be seen from Fig. 5, the ALE method simulated and experimental crack densities on the middle cross section are not close to each other. However, the SPH simulations and experimental results in top, middle and bottom are comparable and match well. It can be further seen from Fig. 5 that at all the three cross sections of the rock cylinder, the crack densities around the borehole are much higher than those at distances far from the borehole. This is not surprising since the rock adjacent to the borehole experiences higher stress intensity.

Figure 6 shows the differences of the simulated crack densities between the air coupling with copper and air coupling without copper cases. The difference in crack density between the two cases seems to be marginal at the top section of the specimen, while a noticeable difference is observed at the middle and bottom sections closer to the borehole. The simulated damage level for the air coupling without copper case is much higher than that of the air coupling with copper case. The difference in crack densities for these two simulations is mainly due to the extra kinetic and plastic strain energies that are absorbed by the copper as a liner.

Figure 7 shows the crack density differences between the air coupling with copper and water coupling with copper simulations. As can be seen from Fig. 7, the crack density is much higher for the water coupling case than that for the air coupling case. This is expectable since water serves as an excellent medium for the transmission of shock waves, in comparison with air.

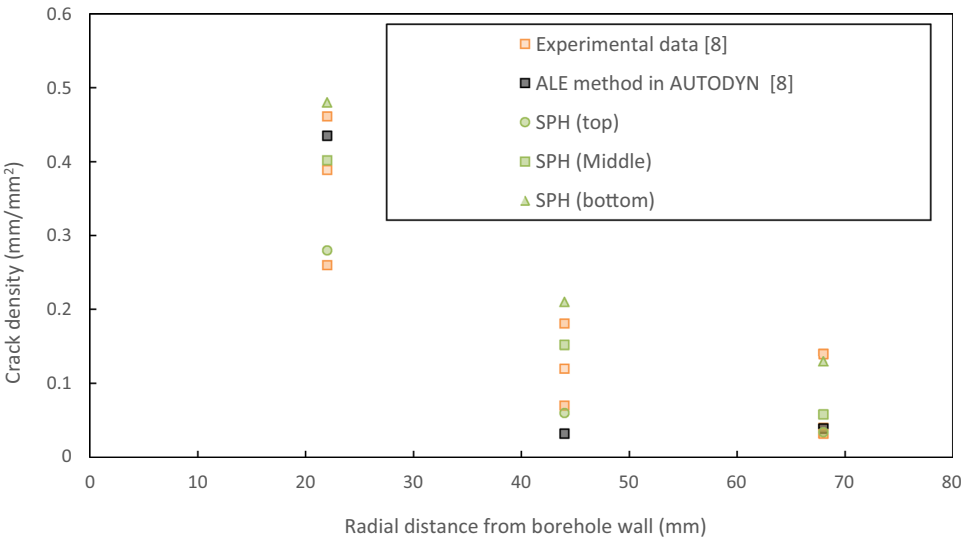

Fig. 5 Crack density distribution in the radial direction at the bottom, middle and top sections of the rock cylinder obtained in the experiment [8] and SPH simulation

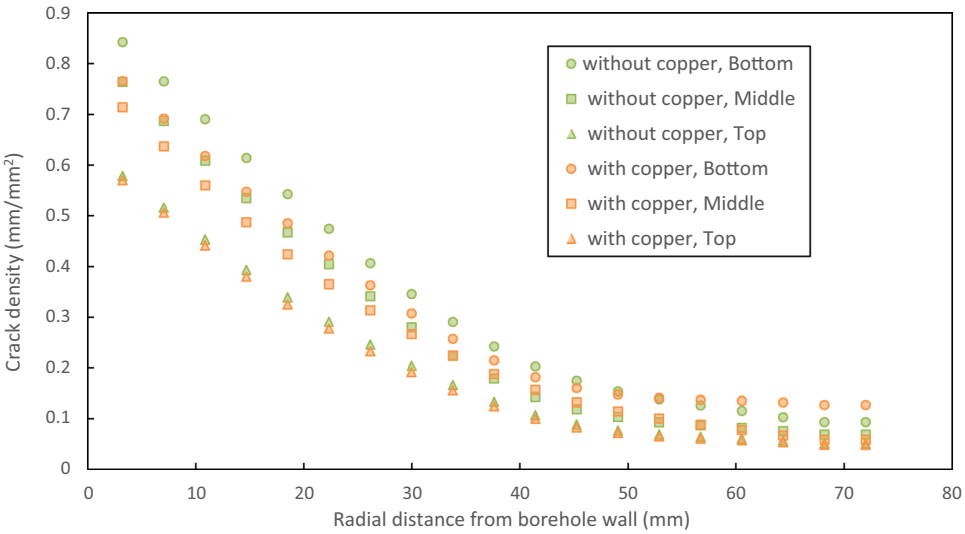

Fig. 6 Crack density distribution in the radial direction at the bottom, middle and top sections of the rock cylinder obtained from the air coupling with and without copper cases

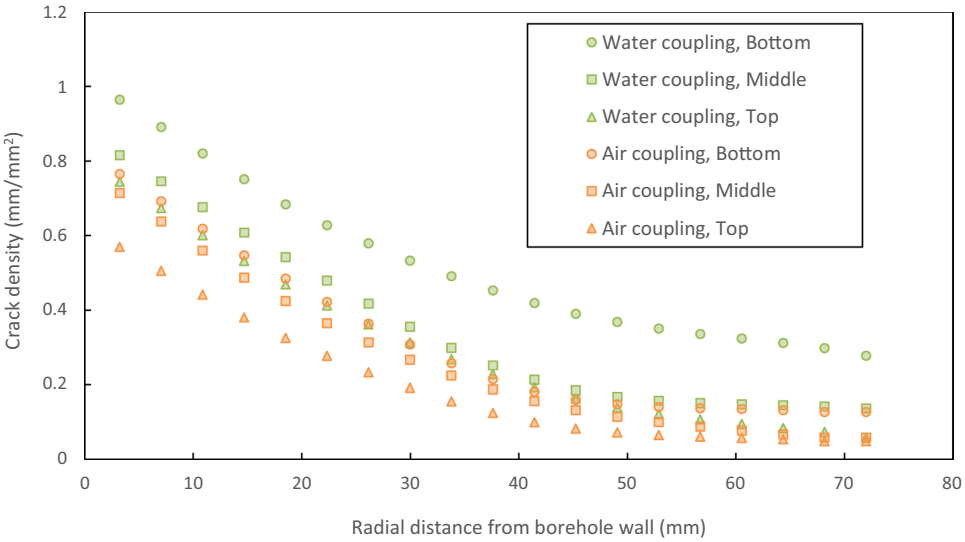

Fig. 7 Crack density distribution in the radial direction at the bottom, middle and top sections of the rock cylinder obtained for air coupling with copper and water coupling with copper

We use the concept of crack distribution probability to give us information about the time evolution of the damage level and the symmetric condition of the damage pattern around the borehole. Crack distribution probability is evaluated using a function based on the number of damaged particles and their damage level in the radial direction. To calculate the crack distribution probability, the radial cross section is evenly divided into 72 axi-symmetrical bins in the loop direction. The summation of each particle's damage level that is above 0.8 in each bin is divided by the total number of particles in that cross section, as expressed below:

$$\mathrm{PDF} = \frac{\sum_i^{n_{D>0.8}} D_i}{\sum_j^{72} n_{\mathrm{bin},j}}, \tag{22}$$

where PDF is probability distribution function in each bin, $n_{D>0.8}$ is the number of particles with damage level higher than 0.8 in each bin and $n_{\mathrm{bin},j}$ is the number of particles in the jth bin. Figure 8 shows the polar graphs which compare the crack distribution probability for the air coupling with copper, air coupling without copper and water coupling with copper cases at simulation time $t = 23$ µs, 69 µs and 145 µs. It can be clearly seen that at $t = 23$ µs the probability fluctuates slightly around the borehole for all three simulations. At $t = 69$ µs, the probability varies considerably around the borehole for all three cases. However, all the distributions still show a somehow symmetrical pattern around the borehole. At time $t = 145$ µs, the probability distribution shows a clear asymmetrical pattern around the borehole for all the three simulations. This is mainly due to the reflection, and superposition of stress waves. The result is the generation of more and more cracks, and finally forming a complicated crack network [15]. At the time between 69 µs and 145 µs, the compressive stress wave changes to a tensile stress wave

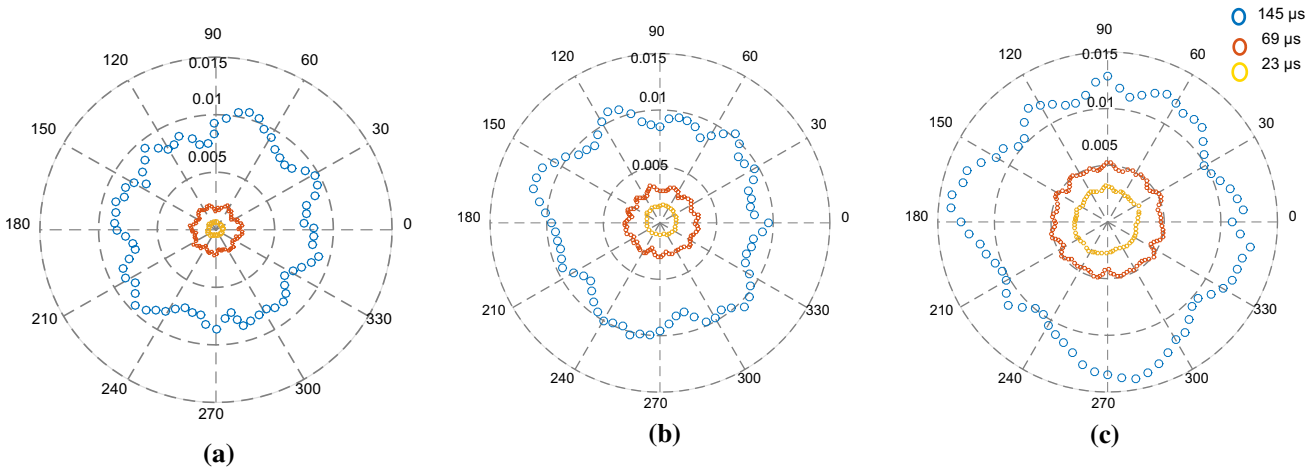

Fig. 8 Crack distribution probability: **a** air coupling with copper, **b** air coupling without copper, and **c** water coupling with copper

at the free surface of the cylindrical rock and returns back into the rock. This reflection as tensile wave affects the crack patterns. It can be seen from Fig. 8 that the shapes of the resulting probability distributions at these two times are quite different. The water-coupling with copper case produces the most extended crack distribution probability, while the air-coupling with copper case produces the least. This is consistent with the crack density plots shown in Figs. 5, 6 and 7.

4 Pore network and permeability analysis

4.1 Geometrical analysis of the fractured network

We compare the three pore network structures from the different simulations in terms of pore and throat size distributions and their connectivity. Void element with length of 0.6 mm is the basic elements used to define the void space and detect the geometrical variations and connectivity. The probability of the throat cross-sectional area, pore volume and coordination number for the three simulations is shown in Figs. 9a, b and 10, respectively. The probability is constructed by dividing the number of throats, pores and coordination numbers occurring in the specific size range by the total number of throats, pores and coordination numbers in each simulated fracture network.

As can be seen from Fig. 9, the water coupling with copper case features the larger pore and throat sizes than the other two cases. This could be attributed to the fact that the number of damaged particles in water coupling with copper is greater than those in the other two cases. Therefore, the number of void elements which are considered for pore and throat phase could be larger, while the fewest pores and

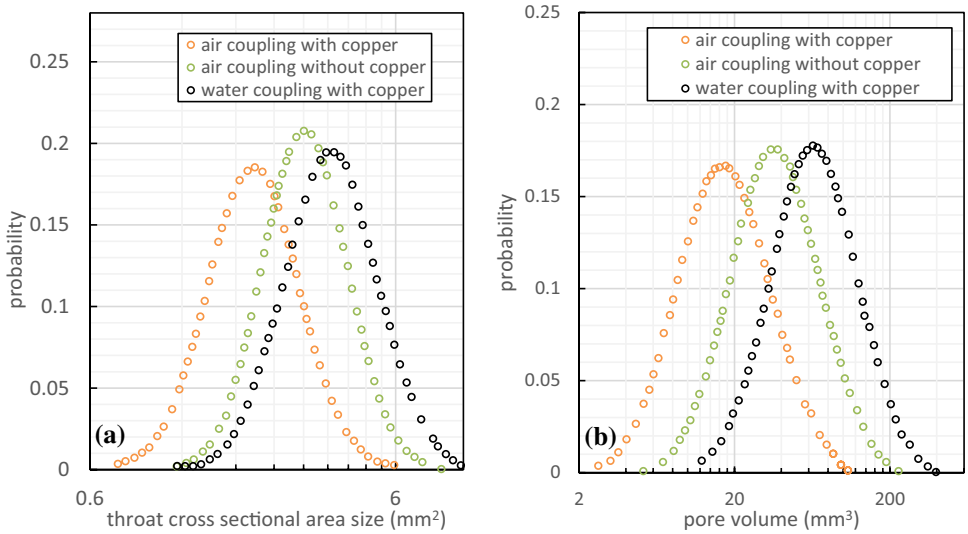

Fig. 9 Distributions of **a** throat cross-sectional area and **b** pore volume obtained from the different fractured networks

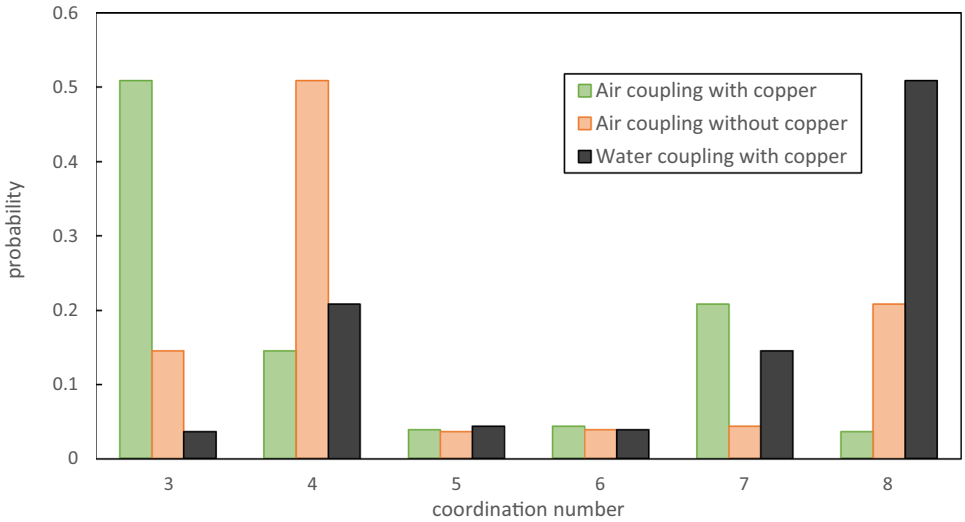

Fig. 10 Distributions of coordination number obtained from the different pore networks

Table 4 Geometry extraction results for the three simulations

Simulations	Air-coupling with copper	Air-coupling without copper	Water-coupling with copper
Open porosity	5.1%	7.4%	15.7%
Total porosity	8.4%	12%	16.3%
Number of percolation pathway			
Radial direction	7	10	18
Axial direction	1	3	5

throats are found in the fracture network in the air coupling with copper case.

Another important topological parameter for the flow properties is the coordination number. It is defined as the number of branches meeting at one pore in the fracture network. As can be seen from Fig. 10, the fracture networks generated in the water coupling with copper case feature more pores with higher coordination numbers, while the air coupling with copper specimen shows the lowest void space connectivity. Overall, Figs. 9a, b and 10 reveal a trend for the three SPH simulations that the coordination number increases as the pore and throat sizes increase.

Table 4 gives the total and open porosity, and percolation pathway studied for the three simulations described in Table 2. The total volume of the pores accounts for the rock porosity, larger pore volume resulting in higher porosity in the blasted specimens, while the dimensions and connectivity of the throats control the flow properties. The air coupling with copper case shows lower porosity and its pore system appears to be much less connected, and its interconnecting throats are more narrow and less numerous (see Table 4) than those of the other two cases. All pores in the whole network for the water coupling with copper case are well interconnected as the calculated values of the total and open porosity are nearly the same.

Percolation path modelling is performed to determine the connectivity in the radial and axial directions of the blast-induced fracture networks using OpenFOAM code. Table 4 depicts the number of the oriented and well-connected fractures along the axial and radial direction connecting pores with diameter sizes ranging from 3 to 4.5 mm in the specimen. This table is a clear indication of higher permeability in the radial direction as compared to the axial direction. Since the number of perfectly connected fracture networks from the top to the bottom of the borehole in the axial direction is less than that in the radial direction, permeability in the axial direction is expected to be lower. This feature is a clear indication of an anisotropic fracture network in the blasted rock and can be extended to understand the anisotropic fluid flow behaviour in our blasted specimens as outlined in the next section.

Figure 11 reports the simulated flow speed field for both axial and radial flows in the fractured specimen obtained using the water coupling with copper simulation. The different colours indicate the variation of the flow speed in the blast-induced fractured rock media. As can be seen from Fig. 11, the majority of the flow speed field is in the range from moderate (green colour) to high (red colour) for the radial flow, and very low (blue colour) to moderate (green colour) magnitude for the axial flow. It can be also observed that velocity is not uniformly distributed.

The permeability of the fractured media depends mainly on the total volume of fractures and their connectivity in the direction of flow. In Fig. 11, the fractures oriented normal to the borehole are more conductive. In particular, it seems that the well-connected fractures in the radial direction enhance

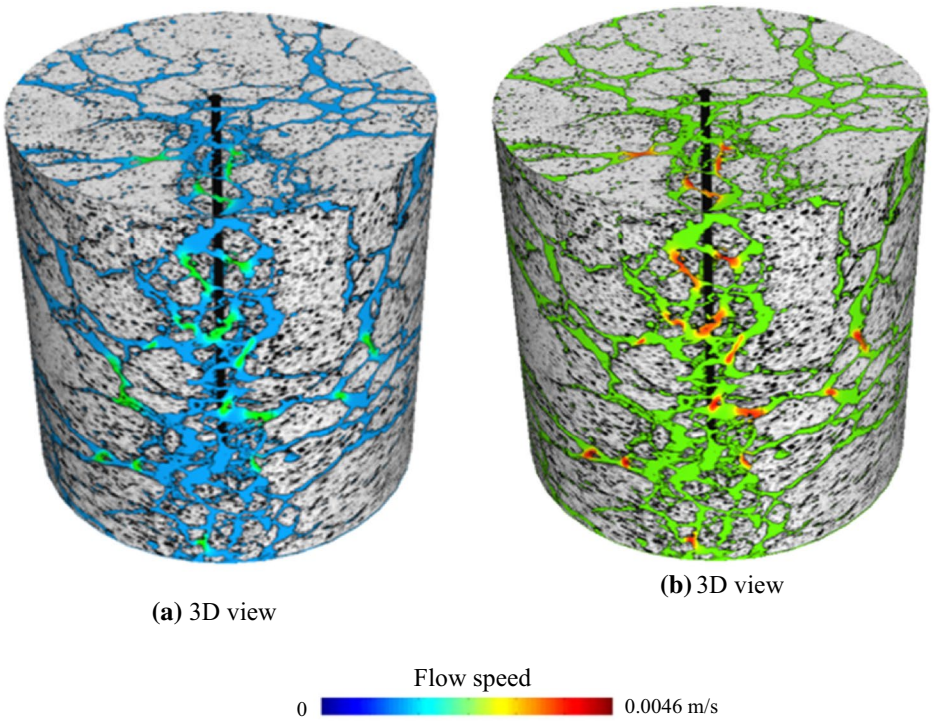

(a) 3D view **(b)** 3D view

Fig. 11 The velocity magnitude field of the **a** axial and **b** radial direction flow in the fractured network obtained using the water coupling with copper simulation. (Colour figure online)

Table 5 Calculated permeability values for the three blast simulations

Simulations	Radial direction k_{rr} (Darcy)	Axial direction k_{zz} (Darcy)
Air-coupling with copper	0.186	0.157
Air-coupling without copper	0.194	0.168
Water-coupling with copper	0.423	0.383

the flow rate significantly in comparison with that in the axial direction.

Table 5 shows the calculated permeability of the fractured networks obtained from the three blast simulations described in Table 2. As can be seen from Table 5, the permeability in the radial direction is higher than that in the axial direction in all the three cases. This observation indicates that the blast-induced fractured specimen has a highly connected pore network in the radial direction, see also Fig. 10.

The reduction in permeability from the radial to axial flow directions is 16%, 13.5% and 9.3% for the air coupling with copper, air coupling without copper and water coupling with copper cases, respectively. The air coupling with copper case shows less permeability. In this case, the smaller pore volumes in the network are poorly connected. This is consistent with the slightly lower coordination numbers of the pores indicating fewer paths available for water to flow. Because of the high connectivity in the fracture network generated in the water coupling with copper simulation, the permeability differences in the radial and axial directions are less than that in the other two cases.

5 Conclusions

This research study adopts an integrated computational approach that permits the prediction of 3D fractured network in Barre granite generated under blast loading using SPH and their resulting permeability using CFD code. It is shown that the adopted SPH method with the JH2 constitutive model is very efficient in reproducing the fractured network of blast-induced rock. Detonation pressure history, detonation pressure profile and crack density distributions are quantitatively in good agreement with experimental data.

Besides, the implementation of a three-dimensional geometry of blast-induced fractured rock using SPH provides us with the essential input to obtain, at the pore scale, both geometrical fractured network parameters and fluid flow properties. The results illustrate that the distribution of fractured network geometry and fluid flow velocity within the simulation domain is highly anisotropic. The radial permeability is higher than the axial permeability owing to the highly pore network connectivity in the radial direction. Significant geometric and topological differences are seen for varying blast design scenarios owing to the effects of coupling materials (e.g. air and water) and copper liner for the Barre granite rock.

Acknowledgements The work was supported in part by the Australian Research Council through Discovery Projects (DP140100945 and DP170102886) and by the National Natural Science Foundation of China (Grant no. 11232003). This research was undertaken with the assistance of resources and services from the National Computational Infrastructure (NCI), which is supported by the Australian Government.

References

1. Sarbhukan MM (1990) Application of bore-blast technique for rock fracturing for drinking water: a case study of Ghotkarwadi, Taluka Akole District Ahmednagar. In: Proceedings of national seminar on modern techniques of rain water harvesting, water conservation and artificial recharge for drinking water, afforestation, horticulture and agriculture, Government of Maharashtra (India)
2. Li W, Xue Z (2000) A review of gas fracturing technology. In: SPE, international petroleum conference and exhibition, Villahermosa, Mexico
3. Guo B, Shan J, Feng Y (2014) Productivity of blast-fractured wells in liquid-rich shale gas formations. J Nat Gas Sci Eng 18:360–367
4. Miller JS, Johansen RT (1976) Fracturing oil shale with explosives for in situ recovery. Bartlesville Energy Research Centre, Bartlesville, Okla. 74003. Advances in Chemistry. American Chemical Society, Washington, DC
5. Austin CF, Leonard GW (1973) Chemical explosive stimulation of geothermal wells. Geothermal energy resources, production and stimulation. Stanford University Press, Stanford, pp 269–292
6. Zhu WC, Wei CH, Li S, Wei J, Zhang MS (2013) Numerical modelling on destress blasting in coal seam for enhancing gas drainage. Int J Rock Mech Min Sci 59:179–190
7. Mokfi T, Shahnazar A, Bakhshayeshi I, Mahmodi Derakhsh A, Tabrizi O (2018) Proposing of a new soft computing based model to predict peak particle velocity induced by blasting. Eng Comput 34:881–888
8. Dehghan Banadaki MM (2010) Stress-wave induced fracture in rock due to explosive action. Ph.D. Dissertation, University of Toronto
9. Nasseri MHB, Rezanezhad F, Young RP (2011) Analysis of fracture damage zone in anisotropic granitic rock using 3D X-ray CT scanning techniques. Int J Fract 168:1–13
10. Alañón A, Cerro-Prada E, Vázquez-Gallo J, P.Santos M A (2018) Mesh size effect on finite element modelling of blast-loaded reinforced concrete slab. Eng Comput 34:649–658
11. Bendezu M, Romanel C, Roehl D (2017) Finite element analysis of blast induced fracture propagation in hard rocks. Comput Struct 182:1–13
12. Potyondy D, Cundall P, Sarracino R (1996) Modelling of shock- and gas-driven fractures induced by a blast using bonded assemblies of spherical particles. In: Mohanty B (ed) Rock fragmentation by blasting. A A Balkema, Rotterdam, pp 55–62
13. Pramanik R, Deb D (2015) Implementation of smoothed particle hydrodynamics for detonation of explosive with application to rock fragmentation. Rock Mech Rock Eng 16:92–99
14. An HM, Liu HY, Han H, Zheng X, Wang XG (2017) Hybrid finite-discrete element modelling of dynamic fracture and resultant fragment casting and muck-pilling by rock blast. Comput Geotech 81:322–345
15. Trivino LF, Mohanty B (2015) Assessment of crack initiation and propagation in rock from explosion-induced stress waves and gas expansion by cross-hole seismometry and FEM–DEM method. Int J Rock Mech Min Sci 77:287–299
16. Fakhimi A, Lanari M (2015) DEM–SPH simulation of rock blasting. Comput Geotech 55:158–164
17. Mishra BK, Murty CVR (2001) On the determination of contact parameters for realistic DEM simulations of ball mills. Powder Technol 115:290–297
18. Belytschko T, Lu YY, Gu L (1995) Element-free Galerkin methods for static and dynamic fracture. Int J Solids Struct 32:2547–2570
19. Wang D, Li Z, Li L, Wu Y (2011) Three dimensional efficient mesh free simulation of large deformation failure evolution in soil medium. Sci China Technol Sci 54:573–580
20. Vignjevic R, Campbell J (2009) Review of development of the smooth particle hydrodynamics (SPH) method. In: Hiermaier S (ed) Predictive modeling of dynamic processes. Springer, Boston, MA, pp 367–396
21. Dautriat J, Gland N, Guelard J, Dimanov AL, Raphanel J (2009) Axial and radial permeability evolutions of compressed sandstones: end effects and shear-band induced permeability anisotropy. Pure Appl Geophys 166:1037–1106
22. Heiland J (2003) Laboratory testing of coupled hydro-mechanical processes during rock deformation. Hydrogeol J 11:122–141
23. Fourar M, Radilla G, Lenormand R, Moyne C (2004) On the non-linear behaviour of a laminar single-phase flow through two and three-dimensional porous media. Adv Water Resour 27:669–677
24. Newman MS, Yin X (2013) Lattice Boltzmann simulation of non-Darcy flow in stochastically generated 2D porous media geometries. SPE J 18:12–26
25. Thauvin F, Mohanty K (1998) Network modelling of non-Darcy flow through porous media. Transp Porous Med 31:19–37
26. Soulaine C, Tchelepi HA (2016) Micro-continuum approach for pore-scale simulation of subsurface processes. Transp Porous Med 113:431–456
27. Javadi M, Sharifzadeh M, Shahriar K (2010) New geometrical model for non-linear fluid flow through rough fractures. J Hydrol 389:18–30
28. OpenFOAM (2015) User guide, version 2.0.0, OpenCFD Ltd, UK. http://www.openfoam.org. Accessed 3 June 2016
29. Guibert R, Nazarova M, Horgue P, Hamon G, Creux P, Debenest G (2015) Computational permeability determination from pore-scale imaging, sample size, mesh and method sensitivities. Transp Porous Med 107:641–656
30. Scanlon TJ, White CK, Borg MC, Palharini R (2015) Open-source direct simulation monte carlo chemistry modelling for hypersonic flows. AIAA J 53:1670–1680
31. Fabritius B, Tabor G (2016) Improving the quality of finite volume meshes through genetic optimisation. Eng Comput 32:425–440
32. Dong H, Blunt MJ (2009) Pore network extraction from micro computerized tomography images. Phys Rev E 80:1–11
33. Jung HB, Kabilan S, Carson JP, Kuprat AP, Um W, Martin PF, Dahl M, Kafentzis T, Varga T, Stephens S, Arey B, Carroll KC, Bonneville A, Fernandez CA (2014) Wellbore cement fracture evolution at the cement—basalt caprock interface during geologic carbon sequestration. Appl Geochem 47:1–16
34. Li L, Shen L, Nguyen GD, El-Zein A, Maggi F (2018) A smoothed particle hydrodynamics framework for modelling multiphase interactions at meso-scale. Comput Mech 62:1071–1085
35. Monaghan J (1992) Smoothed particle hydrodynamics. Annu Rev Astron Astrophys 30:543–574
36. LS-DYNA LSTC (2015) Keyword user's manual, Version R9.0.1, Livermore Software Technology Corporation, Livermore
37. Gray JP, Monaghan JJ, Swift RP (2001) SPH elastic dynamics. Comput Methods Appl Mech Eng 190:6641–6662
38. Liu MB, Liu GR (2010) Smoothed particle hydrodynamics (SPH): an overview and recent developments. Arch Comput Methods Eng 17:25–76

39. Johnson GR, Holmquist TJ (1999) Response of boron carbide subjected to large strains, high strain rates, and high pressures. J Appl Phys 85:8060–8073
40. Ranjan R (2007) Dynamic compression measurements on selected granitic rocks using split Hopkinson pressure bar test. M.A.Sc. Dissertation, University of Toronto
41. Johnson GR, Cook WH (1985) Fracture characteristics of three metals subjected to various strains, strain rate, temperatures and pressures. Eng Fract Mech 21:31–48
42. Boisvert JB, Manchuk JG, Neufeld C, Niven EB, Deutsch CV (2012) Micro-modelling for enhanced small scale porosity–permeability relationships. In: Abrahamsen P, Hauge R, Kolbjornsen O (eds) Geostatistics. Springer, Dordrecht